Advances in Geo-Energy Research

Vol. 20, No. 2, p. 114-128, 2026

Original article

Spatially resolved normal and shear loading beneath stabilised filter-beds on a plain-weave standalone screen

Razqan Razak, Paula A. Gago, Zhixi Chen, Stephen Tyson, Sheikh S. Rahman*

School of Minerals and Energy Resources Engineering, University of New South Wales, Sydney NSW 2052, Australia

Keywords:
Stabilised filter-bed
immersed boundary computational fluid dynamics-discrete element method
normal and shear stress
hotspot mapping
exceedance statistics
standalone sand screen

Cited as:
Razak, R., Gago, P. A., Chen, Z., Tyson, S., Rahman, S. S. Spatially resolved normal and shear loading beneath stabilised filter-beds on a plain-weave standalone screen. Advances in Geo-Energy Research, 2026, 20(2): 114-128.
https://doi.org/10.46690/ager.2026.05.02

Abstract:
Premium standalone sand screens must limit sand production while preserving productivity, yet most erosion- and plugging-centred studies do not quantify how a stabilised filter-bed transfers hydraulic loading into stresses on woven wires. This study quantifies sustained normal and shear loading on a plain-weave standalone screen beneath stabilised sand filter-beds using an immersed boundary computational fluid dynamics-discrete element framework under increasing imposed pressure drop. Screen-surface stresses were evaluated over the loaded screen area for the whole screen and for interior and perimeter reporting zones using area-time-weighted distributions. The results show a clear monotonic strengthening of the stabilised loading state as pressure drop increased. Typical loading rose in both the normal and shear components, with the normal component remaining dominant throughout. The loaded-area fraction increased only modestly, whereas the mean stress over the loaded area increased much more strongly. This indicates that higher pressure drop amplified stress intensity within already engaged regions more than it expanded the area carrying load. The upper tail of the stress distribution also strengthened, which shows that increasing pressure drop intensified not only the typical loading state but also the most severe loading regime. Hotspot maps further showed persistent wire-scale organisation within each stabilised window, together with perimeter-associated amplification in the normal upper tail under the present configuration. These findings provide mechanics-based loading descriptors that can support screen qualification procedures and operating-envelope assessment under stabilised filter-bed loading.

1. Introduction

Sand-screen selection is an energy-engineering design problem that requires simultaneous consideration of sand control, hydraulic productivity, and structural reliability over service life (Wong et al., 2003; Ahad et al., 2020; Abduljabbar et al., 2024). In practice, selection depends on formation and production conditions, particle-size distribution, fluid properties, screen type and material, completion context, and plugging and retention performance (Ahad et al., 2020; Abduljabbar et al., 2024). Wells must also be operated within an appropriate envelope because production rate must be balanced against the risk of impairing or failing the sand-control completion (Wong et al., 2003). Such a balance is important because a screen that retains sand acceptably can still fail under plugging, localised high-velocity flow, erosion, collapse, or related integrity threats (Hamid and Ali, 1997; Wong et al., 2003; Abduljabbar et al., 2024). Mechanical failure during completion or production therefore shows that hydraulic efficiency alone is not a sufficient basis for screen selection, and that integrity must be considered explicitly rather than treated as a secondary consequence of retention performance (Hamid and Ali, 1997; Arukhe et al., 2005).

Much of the published literature remains centred on erosion. Experimental and computational studies show that local

Yandy Scientific Press

*Corresponding author.
E-mail address: razqanrazak@gmail.com (R. Razak); paulaalejandrayo@gmail.com (P. A. Gago); zhixic@unsw.edu.au (Z. Chen); profstevetyson@protonmail.com (S. Tyson); sheik.rahman@unsw.edu.au (S. S. Rahman).

Received February 28, 2026; revised March 25, 2026; accepted April 13, 2026; available online April 16, 2026.

velocity, solids loading, particle size, and screen geometry govern erosion and wear behaviour (Procyk et al., 2015; Ying et al., 2022; Zhou et al., 2022). In gravel-pack and related screen systems, Procyk et al. (2015) linked local flow velocity and solids concentration to erosion-based life estimation and operating guidance. Under blocked and unblocked metal-mesh conditions, Ying et al. (2022) showed that plugging increases local aperture velocity, promotes overcurrent hot spots, and can produce cyclic clogging-dredging behaviour. Zhou et al. (2022) further showed that erosion assessment under bottomhole conditions must account for heterogeneous inflow, confined-space effects, and the competing roles of erosion and annular sand accumulation. Taken together, these studies remain framed primarily in terms of erosion severity, erosion rate, and erosion-based life prediction rather than in terms of spatially resolved normal and shear loading on woven structures. It therefore remains unclear how a stabilised filter-bed transfers sustained hydraulic loading into normal and shear stresses on woven wires and intersections.

Structural-failure evidence shows why this missing mechanics link is crucial. Field and laboratory reports document plugging, collapse, localised damage, productivity loss, and other serious screen failures in compromised intervals (Hamid and Ali, 1997; Arukhe et al., 2005). Qualification studies further show that some premium designs fail burst and collapse requirements below nominal vendor-supplied ratings, and that full-joint performance cannot be inferred reliably from basepipe rating or vendor data alone (Adams et al., 2007). Operational studies also indicate that once partial plugging concentrates flow through a reduced inflow area, the loading environment can evolve rapidly and can leave diagnostic signatures in pressure or surveillance data (Hamid and Ali, 1997; Wong et al., 2003; Arukhe et al., 2005). More broadly, reviews show that screen failure is not governed by erosion alone, because plugging, localised flow hot spots, collapse, corrosion, and related mechanisms can also control survivability (Abduljabbar et al., 2024). However, these studies still do not directly quantify the spatially resolved normal and shear loading imposed on woven mesh by a stabilised filter-bed. The remaining gap is therefore a mechanics gap: How a deposited filter-bed, its sustained pressure drop, and the resulting fluid-particle loading combine to generate a screen-surface stress field that is spatially heterogeneous and potentially relevant to integrity.

This study addresses that gap using an immersed-boundary computational fluid dynamics-discrete element method (CFD-DEM) framework to quantify sustained normal and shear stresses on a plain-weave (PW) standalone screen beneath stabilised sand filter-beds formed under three pressure drops. The modelling basis follows the previously validated framework of Razak et al. (2024), which established the importance of the bulk filter-bed in long-term retention and retained permeability, but the present work focuses on the resulting stress field on the screen surface. For each pressure-drop case, a long-term sand-retention simulation begins from a clean screen and evolves until a stabilised filter-bed regime is identified using a deterministic particle-kinematic criterion. Stress analysis is then performed over the stabilised time window for the whole screen and for interior and perimeter reporting zones. The post-processing quantifies loaded-area recruitment, mean loaded stress, central and upper-tail distributional descriptors, threshold exceedance, and hotspot organisation for both the normal and shear components. The aim is to establish a mechanics-resolved link between stabilised filter-bed loading and screen-surface stress descriptors that can support qualification procedures, operating-envelope development, and future coupling to material-specific structural response or damage models.

2. Materials and methods

This study uses a previously validated immersed-boundary CFD-DEM framework to quantify stabilised normal and shear loading on a PW standalone screen under three imposed pressure drops. The fluid phase is solved in OpenFOAM, particle motion is solved in LIGGGHTS, and coupling is handled through the open-source software of CFDEM project, that is, CFD-DEM project (DCS Computing GmbH, 2013). LIGGGHTS, which stands for LAMMPS improved for general granular and granular heat transfer simulations, is used in the same configuration as in the previously validated studies of Razak et al. (2024, 2025). LAMMPS denotes the Large-scale Atomic/Molecular Massively Parallel Simulator. The present work retains the same numerical framework, material inputs, contact parameters, and screen geometry so that differences in reported loading arise from the imposed pressure drop and the stabilised filter-bed configuration rather than from changes in model setup. For each case, the coupled simulation begins from a clean screen and proceeds until a stabilised filter-bed regime is identified using a deterministic particle-kinematic criterion defined in Section 3.1. Screen stresses are then sampled over the stabilised time window at the same imposed pressure drop. The reconstructed loading field combines resolved fluid traction and particle-screen contact forces and is reported for the whole screen and for the defined reporting zones.

2.1 Sand properties and size distribution

The particulate phase consists of the same non-cohesive river sand used in Razak et al. (2024). The particle-size distribution spans 120 to 630 μm with a modal diameter near 275 μm. This distribution, selected previously for the 180 μm nominal-aperture PW screen, is retained unchanged here; the corresponding particle-size distribution is provided in Fig. S1. Sand grains are represented as spheres with a bulk density of 1,660 kg/m^3. This gives a controlled coarse, predominantly rounded baseline and does not resolve strong angularity, cohesive fines, abrasion-generated ultra-fines, or particle breakage.

The carrier phase is single-phase water treated as an incompressible Newtonian fluid with density 1,000 kg/m^3 and kinematic viscosity 9.6×10^{-7} m^2/s. These properties remain fixed across cases so that observed differences arise from imposed pressure drop and stabilised particle configuration rather than from changes in fluid properties. The present results should therefore be interpreted as loading descriptors

for this controlled baseline, not as universal predictions for all formation sands.

2.2 Immersed boundary method and solver execution

Solver execution follows the previously validated framework introduced above. The present subsection summarises the discretisation, immersed-boundary implementation, and numerical solution procedure used for the pressure-drop sweep.

The fluid phase is discretised with the finite-volume method, and particle motion is advanced with a soft-sphere discrete element formulation. The implementation follows the resolved CFD-DEM framework reported by Goniva et al. (2009, 2010), Kloss et al. (2012), and Hager et al. (2011, 2012, 2014). Particles and plain-weave screen wires are represented through an immersed boundary method in which solid bodies are embedded in a fixed Eulerian grid. A void-fraction field α is defined in every computational cell, where $\alpha = 0$ denotes a fully solid cell, $\alpha = 1$ denotes a fluid-only cell, and $0 < \alpha < 1$ denotes a partially filled cell. Momentum forcing is then applied in cells intersected by particles or wires so that the local fluid velocity satisfies the no-slip condition at solid surfaces. Because particles and wires are embedded in a fixed Cartesian grid, body-fitted meshes and mesh deformation are not required. This approach is consistent with the general immersed-boundary framework reported by Peskin (2002), Taira and Colonius (2007), and Shirgaonkar et al. (2009).

Each global time step advances through a CFD-DEM coupling loop. The fluid solver first updates pressure and velocity using the current immersed-boundary forcing field. The DEM solver then updates particle positions and velocities under hydrodynamic forces, gravity, and grain-grain and grain-wire contacts. The void-fraction field and immersed-boundary forcing terms are recomputed from the updated particle configuration, and the coupled fields are exchanged again. This procedure is repeated until the prescribed convergence criteria are satisfied.

Velocity equations are solved with a residual tolerance of 10^{-5}, whereas pressure and immersed-boundary corrections use a tolerance of 10^{-6}. Velocity is solved with a preconditioned bi-conjugate gradient method and a diagonal incomplete LU preconditioner. Pressure and immersed-boundary corrections are solved with a preconditioned conjugate gradient method and a diagonal incomplete Cholesky preconditioner. Pressure-velocity coupling uses the pressure-implicit with splitting of operators (PISO) algorithm with four correctors, and the Courant number remains below 0.7 in all simulations. Iteration proceeds until the residuals of velocity, pressure, and the immersed-boundary velocity correction satisfy the prescribed tolerances. Further implementation details are given in Razak et al. (2024).

2.3 Governing equations

2.3.1 IBM governing equations

The governing equations used in this study follow the standard incompressible finite-volume and immersed-boundary formulations adopted in OpenFOAM, with formulation roots in Weller et al. (1998), Peskin (2002), Taira and Colonius (2007), and Shirgaonkar et al. (2009). The fluid phase is treated as an incompressible Newtonian liquid, and particle and screen effects are introduced through an immersed-boundary forcing term on the fixed Eulerian grid. Before application of the immersed-boundary correction, the momentum and continuity equations are written as:

$$\rho \frac{\bar{\mathbf{u}} - \mathbf{u}^{n-1}}{\Delta t} + \rho(\mathbf{u}^{n-1} \cdot \nabla)\mathbf{u}^{n-1} = -\nabla \bar{p} + \mu \nabla^2 \mathbf{u}^{n-1} \quad (1)$$

$$\nabla \cdot \bar{\mathbf{u}} = 0 \quad (2)$$

where ρ is the fluid density, μ is the dynamic viscosity, Δt is the time-step size, $\bar{\mathbf{u}}$ is the intermediate velocity field at the current time step, $\mathbf{u}^{n-1}$ is the velocity field at the previous time step, and $\bar{p}$ is the corresponding intermediate pressure field. The equations are advanced in OpenFOAM with pressure-velocity coupling handled through the PISO algorithm.

Fluid-solid interactions are introduced through an immersed-boundary method. A void-fraction field, representing the local fluid volume fraction, α is defined in every CFD cell. Cells that contain only fluid have $\alpha = 1$, whereas cells intersected by particles or screen wires have $\alpha < 1$. In cells with $\alpha < 1$, an immersed-boundary forcing term drives the local fluid velocity towards the velocity of the intersecting solid phase. This immersed-boundary forcing vector $\mathbf{f}$ is written as:

$$\mathbf{f} = \rho \frac{\bar{\mathbf{u}}_c - \bar{\mathbf{u}}}{\Delta t} \quad (3)$$

where $\bar{\mathbf{u}}_c$ denotes the velocity field after immersed-boundary correction. Substituting this forcing into the momentum equation gives the immersed-boundary-modified momentum equation:

$$\rho \frac{\bar{\mathbf{u}}_c - \mathbf{u}^{n-1}}{\Delta t} + \rho(\mathbf{u}^{n-1} \cdot \nabla)\mathbf{u}^{n-1} = -\nabla \bar{p} + \mu \nabla^2 \mathbf{u}^{n-1} + \mathbf{f} \quad (4)$$

The corrected field $\mathbf{u}_c$ does not generally satisfy incompressibility. A scalar correction field θ is therefore obtained from:

$$\nabla^2 \theta = \nabla \cdot \bar{\mathbf{u}}_c \quad (5)$$

Here, θ is the scalar correction field used to restore incompressibility after immersed-boundary forcing has been applied.

The divergence-free velocity at the end of the time step is then defined as:

$$\mathbf{u}^n = \bar{\mathbf{u}}_c - \nabla \theta \quad (6)$$

So that $\nabla \cdot \mathbf{u}^n = 0$ holds throughout the domain. Incorporating the pressure-correction field ϕ which is associated with the PISO step, gives the final immersed-boundary-modified momentum equation:

$$\rho \frac{\bar{\mathbf{u}} - \mathbf{u}^{n-1}}{\Delta t} + \rho(\mathbf{u}^{n-1} \cdot \nabla)\mathbf{u}^{n-1} = -\nabla \left(\bar{p} + \rho \frac{\phi}{\Delta t} \right) + \mu \nabla^2 \mathbf{u}^{n-1} + \mathbf{f} \quad (7)$$

Hydrodynamic-force evaluation follows the resolved pressure-and-viscous-stress treatment and the standard Newto-

Table 1. DEM contact parameters used for particle-particle and particle-screen interactions.

Parameter	Value
Young's modulus (Pa)	1.08×10^8
Poisson's ratio (-)	0.3
Coefficient of friction (-)	0.5
Coefficient of restitution (-)	0.15

nian stress definition used in incompressible flow formulations. Hydrodynamic forces on each DEM particle are obtained from the resolved pressure and viscous stress tensor. For a particle j occupying the corresponding set of CFD cells, the net hydrodynamic force, $\mathbf{F}_j$, is:

$$\mathbf{F}_j = \int_{\Omega_j} (\nabla p - \nabla \cdot \boldsymbol{\tau})\, \mathrm{d}\Omega \tag{8}$$

where Ω_j is the fluid control-volume region occupied by particle j, $\mathrm{d}\Omega$ is the differential volume element, and $\boldsymbol{\tau}$ is the viscous stress tensor for a Newtonian fluid:

$$\boldsymbol{\tau} = \mu \left[\nabla \mathbf{u} + (\nabla \mathbf{u})^T\right] \tag{9}$$

These hydrodynamic forces are passed to the DEM solver and combined with contact forces when particle motion is updated (Razak et al., 2024).

2.3.2 Particle motion, contact model, and material parameters

Particle trajectories are advanced using the soft-sphere DEM formulation implemented in LIGGGHTS (Kloss et al., 2012). Time integration, neighbour search, and CFD-DEM coupling settings follow the retained baseline configuration used in the present simulations.

Contact interactions between particles and between particles and screen wires are described using a soft-sphere model. Normal contact forces follow a Hertzian elastic law with viscous damping, consistent with Hertz-type contact mechanics and its granular extensions (Brilliantov et al., 1996). Tangential forces include an elastic component and are limited by a Coulomb friction criterion, in line with standard soft-sphere DEM practice (Cundall and Strack, 1979). The same contact model is retained across all pressure-drop cases, so differences in screen loading arise from the imposed pressure drop and the stabilised filter-bed structure, while contact physics remain unchanged.

Mechanical parameters for particle-particle and particle-screen contacts are listed in Table 1. The measured particulate inputs and DEM contact parameters are retained from the previously validated PW baseline configuration, so that differences between pressure-drop cases arise from the imposed pressure drop and the stabilised filter-bed structure, while material and contact inputs remain fixed. These parameters determine the magnitude of grain-grain and grain-wire forces and therefore influence the stress levels transmitted to the screen wires.

The quantities used in the particulate phase fall into three categories. The sand density and particle-size distribution are experimentally characterised inputs inherited from Razak et al. (2024). The spherical particle shape is a modelling abstraction chosen to remain consistent with the predominantly rounded river sand used in that validated baseline. By contrast, Poisson's ratio, coefficient of friction, coefficient of restitution, and Young's modulus are DEM contact parameters retained from the previously validated soft-sphere configuration and were not re-measured as material properties for the present pressure-drop sweep. In particular, the Young's modulus value should be interpreted here as an effective contact stiffness used within the Hertz-Mindlin DEM formulation to preserve stable and consistent contact-force transmission across cases, not as a new direct laboratory measurement of the intrinsic elastic modulus of the grains. The DEM time step is then calculated from the Rayleigh criterion using the same conservative scaling retained across the present cases.

2.3.3 Screen-stress reconstruction on the screen

Screen-surface loading is reconstructed from the triangulated STL representation and the facet-wise force accumulation returned by the LIGGGHTS 'mesh/surface/stress' module, consistent with the LIGGGHTS documentation (DCS Computing GmbH, 2013). The PW screen is represented as a triangulated surface imported from an STL file. Each triangle i has centroid position $\mathbf{x}_i$, unit normal vector $\mathbf{n}_i$, and area A_i. These STL facets are treated as the elementary surface units for all screen-stress calculations.

Screen loading from the granular assembly is evaluated using the LIGGGHTS mesh module "mesh/surface/stress". For every contact between a DEM particle and triangle i, where i is the STL facet index, the DEM contact model returns the particle-contact force vector $\mathbf{g}_i^{(k)}$ exerted on the mesh during contact k, where k is the contact index. The mesh module accumulates the net force vector on facet i by summing all particle-contact force vectors over the contact set assigned to that facet:

$$\mathbf{F}_i = \sum_{k \in \mathscr{C}_i} \mathbf{g}_i^{(k)} \tag{10}$$

where $\mathscr{C}_i$ denotes the set of particle contacts associated with facet i during the current coupling step, $\mathbf{g}_i^{(k)}$ is the contact-force vector arising from contact k on facet i, and $\mathbf{F}_i$ is the resulting net force on that facet. Parallel communication yields facet-wise net forces on all STL triangles at each output time.

The net force on each facet is decomposed into normal and tangential components with respect to the STL normal. The normal component on facet i is:

$$\mathbf{F}_{n,i} = (\mathbf{F}_i \cdot \mathbf{n}_i)\, \mathbf{n}_i \tag{11}$$

and the tangential component is:

$$\mathbf{F}_{t,i} = \mathbf{F}_i - \mathbf{F}_{n,i} \tag{12}$$

Here, $\mathbf{F}_{n,i}$ and $\mathbf{F}_{t,i}$ are the normal and tangential components of the net facet force, resolved with respect to the local STL unit normal $\mathbf{n}_i$.

The facet-averaged normal and shear stress magnitudes that

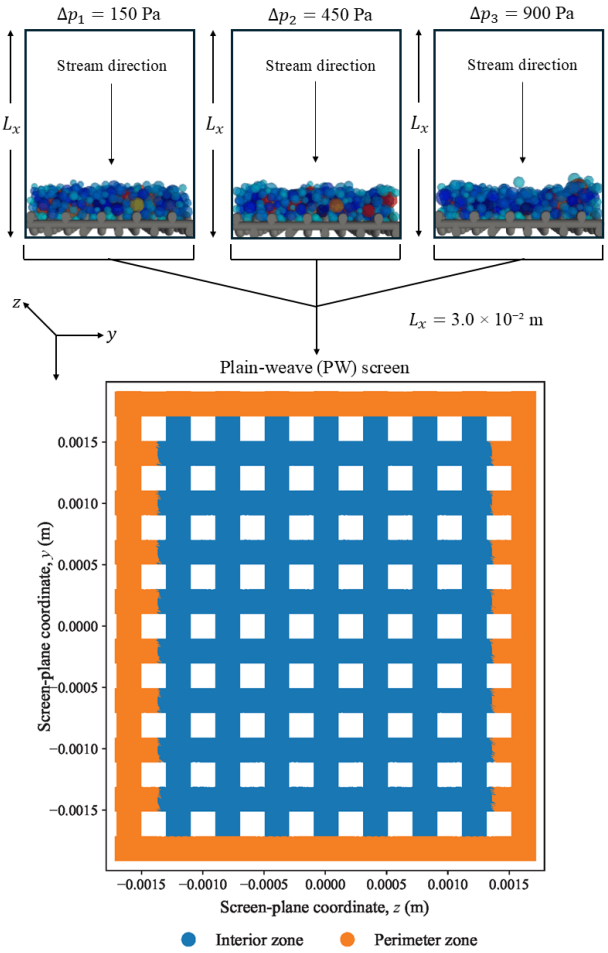

Fig. 1. Computational domain, boundary conditions, and reporting zones for the PW screen under three imposed pressure drops.

are written to the output fields σ_n and σ_t are then:

$$\sigma_n(i) = \frac{\|\mathbf{F}_{n,i}\|}{A_i}, \quad \sigma_t(i) = \frac{\|\mathbf{F}_{t,i}\|}{A_i} \tag{13}$$

All quantities are expressed in the Supplementary file, so σ_n and σ_t have units of Pa. The sign of the scalar normal traction depends on the chosen STL normal orientation. Since the analysis in this study focuses on stress magnitude, σ_n and σ_t are reported as absolute values.

These scalar stress fields are interpreted as contact-induced surface-load descriptors on the PW screen rather than as internal stresses within a deformable screen. Statistical descriptors of σ_n and σ_t used to compare pressure-drop cases are defined in Section 3.

2.4 Computational domain description

The computational domain is a rectangular cuboid of length 3×10^{-2} m in the streamwise direction. Its cross-sectional dimensions in the transverse directions are taken from the PW configuration reported in Razak et al. (2025). The PW screen is positioned at $x = 2.5 \times 10^{-2}$ m and has a nominal aperture width of 180 μm with the same wire diameter and weave definition as the validated baseline configuration. Flow is aligned with the positive x direction. The computational domain, boundary conditions, and reporting zones are shown in Fig. 1. A stabilised sand filter-bed forms upstream of the screen and covers the screen face. Bed thickness is reported as a stabilised-state descriptor using the distance from the screen plane to the outer surface of the deposited filter-bed.

The screen geometry is imported as a triangulated STL surface into OpenFOAM. The background mesh is generated with 'blockMesh' as a structured Cartesian grid with a base cell size of approximately 69 μm, which corresponds to about four cells per modal particle diameter, and is refined locally around the screen using 'snappyHexMesh' in castellation mode. Snapping and layer addition are omitted to preserve compatibility with the immersed-boundary solver and to maintain near-cubic cell shapes. A refinement box centred on the screen restricts the finest cells to the region of interest. Near-screen cell sizes are approximately 17 to 20 μm. This resolution is retained here so that wire-scale stress variations are resolved while the total cell count remains computationally feasible.

Three constant pressure drops are imposed between inlet and outlet boundaries, namely $\Delta p_1 = 150$ Pa, $\Delta p_2 = 450$ Pa, and $\Delta p_3 = 900$ Pa. The corresponding pressure gradients are listed in Table S1. The fluid phase is driven by fixed pressures at the inlet and outlet, and slip boundary conditions are applied on the lateral boundaries to reduce sidewall drag and artificial confinement. For the DEM phase, the domain boundaries and the screen are treated as fixed walls for particle motion. During the retention stage, particles may pass through the screen apertures. During the stabilised stress-sampling stage, no new particles are introduced, and none are removed. For the fluid properties and domain dimensions used here, the flow remains laminar.

The DEM time step is 5×10^{-8} s, the representative CFD time step is 5×10^{-6} s, and the CFD-DEM coupling interval is held constant at 100 CFD steps per DEM update, consistent with the previously validated configuration.

Each case starts from a clean screen and evolves under its imposed pressure drop until a stabilised filter-bed regime is identified. The onset of stabilisation is defined from the deterministic particle-kinematic criterion reported in Section 3.1. The stable reporting window is then taken as $[t_{\text{onset}}, t_{\text{end}}]$, where t_{end} is the final available stress field for the corresponding case. Stress statistics are sampled over that stabilised window at the same imposed pressure drop. Domain dimensions and mean stabilised filter-bed thicknesses are summarised in Table S2. The reporting zones used later in the stress analysis are defined in Fig. 1 and consist of the whole screen, an interior zone, and a perimeter zone. Their exact geometric definition is given in Section 3.

3. Results and discussion

This section quantifies loading-induced stresses on a PW screen beneath stabilised filter-beds for three imposed pressure drops, namely $\Delta p_1 = 150$, $\Delta p_2 = 450$ and $\Delta p_3 = 900$ Pa. The analysis is restricted to stabilised windows so that the reported quantities represent sustained structural loading beneath an established filter-bed. Erosion, material degradation, and geomechanical collapse are outside the present scope. Stresses

are evaluated at individual screen facets and interpreted as spatial distributions over the screen surface.

Two complementary metric families are reported, namely bulk loading metrics and tail metrics. Percentiles Px denote the x-th percentile of the area-time-weighted stress distribution over the loaded area within a reporting zone, where the weighting is proportional to facet area and sampled time within the stabilised window. A facet is classified as loaded when the reported stress magnitude satisfies $\sigma > \sigma_{\min}$. In the present study, $\sigma_{\min} = 0$ Pa because unloaded facets were exported as exact zeros in the stress fields. A sensitivity check using $\sigma_{\min} = 1$ Pa produced negligible changes in the loaded-area fraction, the mean stress over the loaded area, the weighted quantiles, and the exceedance statistics, as shown in Table S3. The conclusions are therefore not sensitive to the zero-threshold definition. In workflows that report small non-zero numerical noise on unloaded facets, $\sigma_{\min}$ should be set above the noise floor. P50 represents the median, P75 the upper quartile, and P99 and P99.5 characterise the upper portion of the distribution.

Following the accounting logic used in contact mechanics, total load may be decomposed into the fraction of area that carries load and the mean stress intensity over that area. Consistent with that logic, the loaded-area fraction, f_L, is defined here as a reporting quantity by:

$$f_L = \frac{A_{\text{loaded}}}{A_{\text{zone}}} \tag{14}$$

where A_{loaded} is the loaded area within the reporting zone and A_{zone} is the total area of that reporting zone. Eq. (14) therefore gives the fraction of zone area carrying non-zero stress. Bulk loading metrics describe the typical stabilised state using P50, P75, f_L, and μ_{active}, where μ_{active} denotes the mean stress over the loaded area (Greenwood and Williamson, 1966; Persson, 2001; Meng et al., 2025).

Tail metrics describe high-stress behaviour using P99, P99.5, and threshold exceedance. This framing is consistent with prior work that characterises broad force or traction distributions through percentile and exceedance-style statistics rather than isolated maxima (van Eerd et al., 2007; Joe et al., 2023). For the present study, exceedance is reported in two equivalent forms. The conditional exceedance over the loaded area is defined as:

$$E_{\text{loaded}}(\sigma \geq T) = \frac{A(\sigma \geq T)}{A_{\text{loaded}}} \tag{15}$$

where T is the chosen stress threshold and $A(\sigma \geq T)$ is the area within the reporting zone for which the stress magnitude equals or exceeds that threshold. The corresponding whole-zone exceedance is defined as:

$$E_{\text{zone}}(\sigma \geq T) = f_L E_{\text{loaded}}(\sigma \geq T) \tag{16}$$

which is equivalently written as:

$$E_{\text{zone}}(\sigma \geq T) = \frac{A(\sigma \geq T)}{A_{\text{zone}}} \tag{17}$$

Eq. (16) makes the decomposition explicit, whereas Eq. (17) shows the same quantity as a direct whole-zone area fraction. Reference thresholds of 2,000 Pa for the normal component and 500 Pa for the shear component are used for cross-case comparisons within the stabilised regime and are reported as $E(\sigma_n \geq 2{,}000 \text{ Pa})$ and $E(\sigma_t \geq 500 \text{ Pa})$. These thresholds act as fixed anchors that lie within the high-stress regime for all cases and yield non-trivial exceedance across zones, while P99 and P99.5 provide threshold-independent confirmation of tail behaviour.

Spatial interpretation is reported for three zones: The whole screen, the interior zone, and the perimeter zone, as shown in Fig. 1.

For spatial reporting in this study, facet centroids were projected onto a best-fit plane obtained from principal component analysis, which defines two in-plane coordinates. The in-plane extents of the projected screen are:

$$L_y = y_{\max} - y_{\min} \tag{18}$$

$$L_z = z_{\max} - z_{\min} \tag{19}$$

where $y_{\min}$ and $y_{\max}$ are the minimum and maximum projected coordinates in one in-plane direction, and $z_{\min}$ and $z_{\max}$ are the corresponding limits in the other. The perimeter zone is then defined as a boundary band of thickness:

$$\delta = 0.10 \times \min(L_y,\ L_z) \tag{20}$$

A facet belongs to the perimeter zone when:

$$d = \min(y - y_{\min},\ y_{\max} - y,\ z - z_{\min},\ z_{\max} - z) \leq \delta \tag{21}$$

where d is the minimum in-plane distance from that facet centroid to the screen boundary. All remaining facets define the interior zone. This zone definition is independent of mesh indexing and processing order, which ensures reproducibility across cases.

A supporting sensitivity check using perimeter-band widths of 5%, 10%, and 15% of the minimum in-plane span is reported in Fig. S4. The 10% and 15% definitions gave the same qualitative conclusion for the normal upper tail, whereas the 5% band under-resolved the engaged perimeter loading zone. The 10% definition was therefore retained as the narrower band that still captured the distributed perimeter-associated loading response. Interpretation therefore focuses on zone-aggregated stress statistics, and no inference is drawn from the exact position of individual hotspot facets. A corner split of the retained 10% perimeter band is used later only to distinguish corner and non-corner perimeter contributions in the normal upper tail.

3.1 Stable window definition

All reported stress statistics are pooled over stabilised filter-bed windows. The purpose of this subsection is to define that window in a deterministic and reproducible way so that cross-case stress comparisons are made only after the deposited bed has reached a mechanically comparable post-deposition regime. The resulting onset identification for the three pressure-drop cases is summarised in Fig. 2. Residual within-window variability is handled through time pooling and through the per-time diagnostics and snapshot selection introduced later. The analysis does not assume strict stationarity of

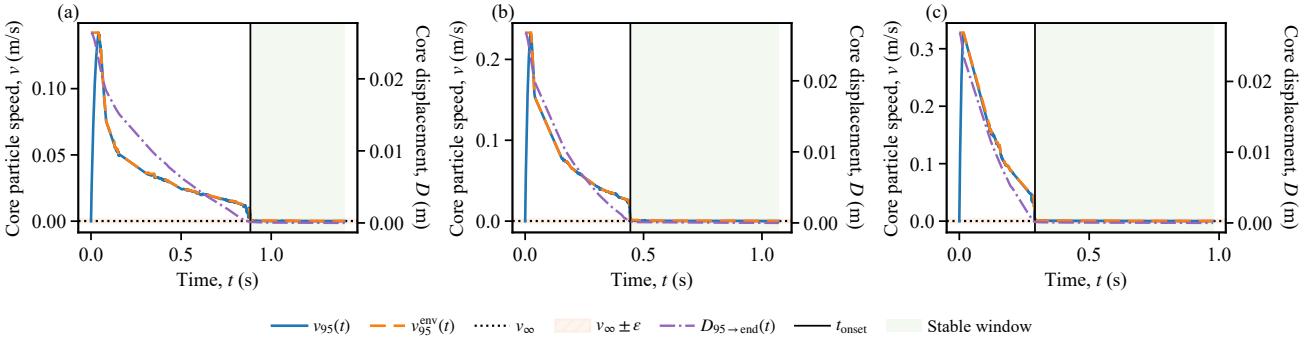

Fig. 2. Stable-window definition from the core-speed plateau rule: (a) Δp_1 onset, (b) Δp_2 onset, and (c) Δp_3 onset.

the stress field within the stabilised window. It instead treats the stable interval as an ensemble of mechanically comparable states.

Pooling begins at the bed-stabilisation onset time, t_{onset}, and ends at t_{end}, which is the final available stress field for the corresponding pressure-drop case. Reported stresses are therefore restricted to loading beneath a kinematically stabilised filter-bed and exclude the earlier deposition and rearrangement phase.

The onset time is determined from particle-bed kinematics extracted from time-resolved DEM outputs. A region of interest is first defined in physical coordinates so that it fully contains the final deposited filter-bed. An inner region is then obtained by uniformly contracting that outer region in order to reduce boundary-induced intermittency and inflow-transition effects. Within this inner region, particles with coordination number $c_{\text{contactno}} \geq 2$ define an operational -bearing skeleton subset. This subset is intended to capture a mechanically connected contact network that governs heterogeneous force transmission in granular materials (Majmudar and Behringer, 2005; van Eerd et al., 2007). Coordination number constrains connectivity within that network and correlates with force-chain statistics (van Eerd et al., 2007; Zhang et al., 2014). Force transmission through such networks is spatially heterogeneous and is typically characterised by a broad force distribution, in which many contacts carry relatively low forces whereas a smaller subnetwork carries disproportionately high forces (Peters et al., 2005; van Eerd et al., 2007).

Stabilisation is assessed relative to an end-anchored reference configuration. For each case, skeleton particles at the final DEM output time define the reference core set. Earlier times are then evaluated relative to that final configuration. Displacement tolerances are normalised by the median core diameter at final time, $d_{50,\ \text{core}}$, which renders the stabilisation criterion dimensionless and comparable across pressure-drop cases.

Two kinematic measures are evaluated. The first is $v_{95}(t)$, which denotes the 95-th percentile of particle-speed magnitude within the operational skeleton subset at time t. The second is $D_{95\to\text{end}}(t)$, which denotes the 95-th percentile of displacement relative to final particle position. These measures quantify residual mobility within the load-bearing network. The use of upper-percentile statistics ensures that stabilisation requires suppression of high-mobility outliers rather than relying on average behaviour alone.

The onset rule used here is introduced as a deterministic post-processing criterion for the present study. It is not taken from a single prior constitutive settling law. Instead, it combines a monotone envelope of the upper-percentile speed statistic with a mixed absolute-relative tolerance rule. The monotone envelope of $v_{95}(t)$ is defined as:

$$v_{95}^{*}(t_i) = \max_{j \geq i} v_{95}(t_j) \tag{22}$$

where t_i is the current sampled time and j spans all later sampled times. Eq. (22) is therefore a reverse cumulative maximum. It removes temporary local reductions in $v_{95}(t)$ and guarantees that once the envelope enters a terminal plateau band, it cannot subsequently exit unless the data are inconsistent.

Let denote the final value of v_{95}^{*}, and let denote its initial value. A tolerance band:

$$\varepsilon = \max(\varepsilon_{\text{abs}}, \alpha(v_0 - v_\infty),\ \beta v_\infty) \tag{23}$$

where ε_{abs} is an absolute tolerance, α scales the total decay magnitude, and β scales the terminal value. Eq (23) is applied identically across cases. The onset time t_{onset} is then taken as the earliest time at which $v_{95}^{*}(t)$ enters and remains within $[v_\infty - \varepsilon,\ v_\infty + \varepsilon]$. This sustained plateau-entry rule prevents temporary local plateaus from being misclassified as stabilisation and enforces a persistent low-mobility condition within the load-bearing skeleton.

For the three pressure-drop cases, the total decay in the monotone envelope is substantial relative to the tolerance band. For Δp_1, $v_0 = 0.1423$ m/s and $v_\infty = 1.05 \times 10^{-4}$ m/s, which gives a total drop of 0.14215 m/s and a tolerance $\varepsilon = 1.42\text{d}-3$ m/s. For Δp_2, $v_\infty = 1.02 \times 10^{-4}$ m/s, the total drop is 0.23299 m/s, and $\varepsilon = 2.33 \times 10^{-3}$ m/s. For Δp_3, $v_\infty = 1.95 \times 10^{-4}$ m/s, the total drop is 0.32786 m/s, and $\varepsilon = 3.28 \times 10^{-3}$ m/s. In all three cases, ε is less than two percent of the total decay magnitude, which indicates that the detected plateau is not controlled by numerical noise.

To compare stabilisation behaviour across the three pressure-drop cases, Fig. 2 summarises the evolution of the core-speed statistic, its monotone envelope, the displacement statistic, and the plateau-based onset selection. The figure

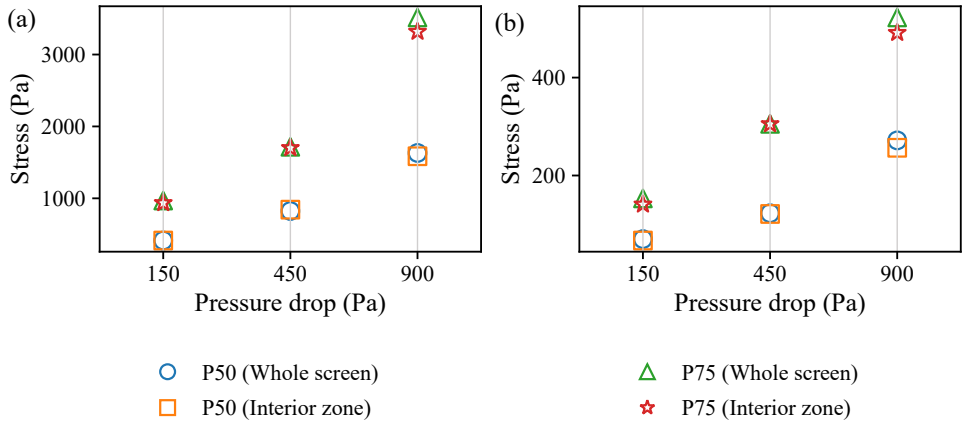

Fig. 3. Typical stabilised loading versus pressure drop for the (a) normal and (b) shear components.

Table 2. Loaded-area fraction and mean loaded stress for the stabilised loading state.

Case	Normal component						Shear component					
	Whole screen		Interior zone		Perimeter zone		Whole screen		Interior zone		Perimeter zone	
	f_L	μ_{active}	f_L	μ_{active}	f_L	μ_{active}	f_L	μ_{active}	f_L	μ_{active}	f_L	μ_{active}
Δp_1	0.0306	6,674	0.0343	6,298	0.0094	14,418	0.0272	1,541	0.0306	1,491	0.0076	2,692
Δp_2	0.0381	11,378	0.0386	12,304	0.0355	5,936	0.0351	3,284	0.0354	3,630	0.0334	1,304
Δp_3	0.0385	21,256	0.0425	20,696	0.0156	29,868	0.0372	4,881	0.0410	4,757	0.0154	6,745

reports $v_{95}(t)$, its monotone envelope $v_{95}^{*}(t)$, the displacement statistic $D_{95\to\text{end}}(t)$, the terminal value v_{∞}, the tolerance band $v_{\infty}\pm\varepsilon$, the selected onset time t_{onset}, and the resulting stabilised window for each case. The selected onset corresponds to sustained suppression of particle mobility, after which the envelope remains within the prescribed tolerance band. The resulting stabilised windows are $[0.884500, 1.408000]$ s for Δp_1, $[0.444250, 1.071500]$ s for Δp_2, and $[0.291250, 0.977675]$ s for Δp_3. The onset time decreases as pressure drop increases, which indicates faster decay of particle mobility under stronger hydraulic forcing. All reported stress statistics are restricted to these windows. This stabilisation rule therefore ensures that cross-case stress comparisons are performed under mechanically comparable filter-bed states.

These durations should be interpreted as simulation times for pore-scale mechanical settling and load redistribution within the deposited filter-bed under the imposed hydraulic forcing. They are not direct predictions of field-scale stabilisation time in oil and gas wells, where inflow conditions, particle supply, formation response, and other coupled processes may continue to evolve over much longer periods. The short reported times are also consistent with the finite laboratory-scale computational domain used here, because both the streamwise travel distance and the spatial extent over which rearrangement must occur are much smaller than in field-scale sand-control systems. The present stable window therefore represents a mechanically settled post-deposition regime within the numerical model and is used only to isolate sustained loading beneath an already established filter-bed.

A coordination-number diagnostic was used as a supporting check on contact-network consistency across the stabilised windows. The corresponding streamwise conditional statistics are reported in Figs. S2 and S3. These diagnostics support the use of $c_{\text{contactno}} \geq 2$ as the operational skeleton definition and do not alter the main stress interpretation.

3.2 Typical stabilised loading state as a function of pressure drop

Within the metric framework defined above, the pressure-drop response of the stabilised loading state is first examined through the bulk loading metrics P50, P75, f_L, and μ_{active}. Fig. 3 summarises the loaded-area percentiles P50 and P75 for the whole screen and the interior zone, and Table 2 reports f_L and μ_{active} for the whole screen, interior zone, and perimeter zone.

To establish the baseline pressure-loading response in the stabilised regime, the typical loading state was first assessed using bulk statistics. Fig. 3 shows that typical stabilised loading increases monotonically with pressure drop for both stress components. For the whole screen, the normal-component P50 increases from 413 Pa at Δp_1 to 824 Pa at Δp_2 and 1,631 Pa at Δp_3, whereas P75 increases from 969 to 1,717 and 3,516 Pa. For the shear component, P50 increases from 70 to 123 and 272 Pa, whereas P75 increases from 153 to 306 and 523 Pa. The ordering $\Delta p_1 < \Delta p_2 < \Delta p_3$ is preserved across all bulk statistics, which establishes a monotonic pressure-

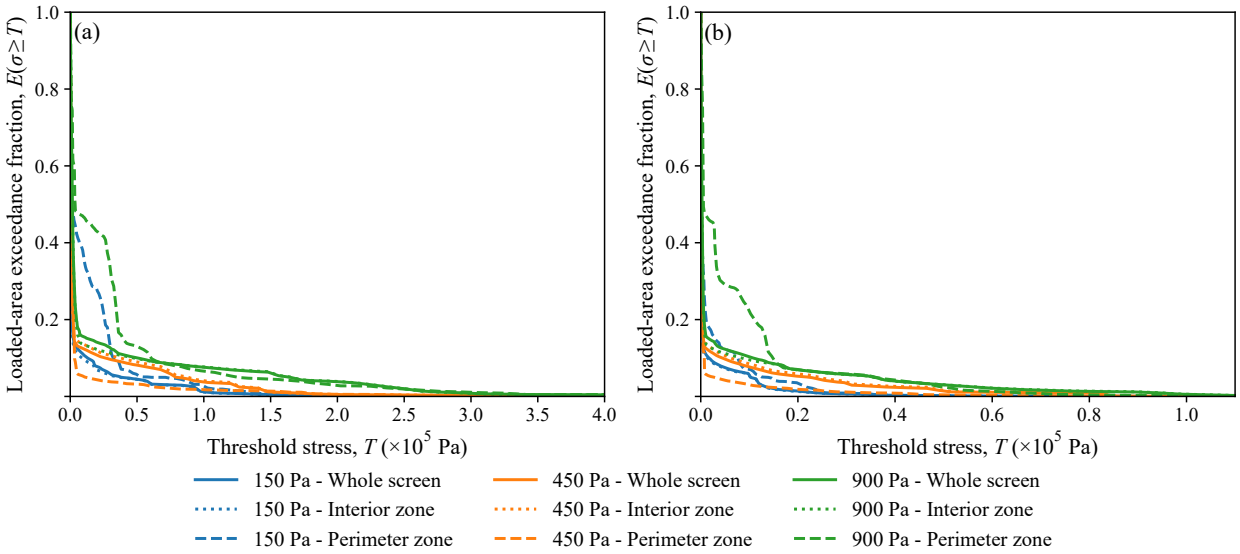

Fig. 4. Loaded-area exceedance curves for stabilised (a) normal and (b) shear stress.

loading hierarchy before examination of tail behaviour and spatial organisation.

Typical loading is also clearly normal-dominated. For the whole screen, the normal-component P50 is about six times larger than the shear-component P50 across the three pressure drops, and a comparable separation is retained at P75. This component hierarchy reappears later in the exceedance, upper-tail, and hotspot-map results.

The interior zone closely tracks the whole-screen percentiles. For the normal component, interior-zone P50 increases from 413 to 842 and 1,585 Pa, whereas P75 increases from 935 to 1,700 and 3,318 Pa. For the shear component, interior-zone P50 increases from 67 to 121 and 257 Pa, whereas P75 increases from 141 to 305 and 492 Pa. The near coincidence of whole-screen and interior statistics indicates that the conditional bulk response is governed primarily by the interior zone under the present zone definition. This provides the baseline against which perimeter-associated upper-tail behaviour is evaluated later.

To separate growth in loaded-area coverage from growth in stress intensity, the loaded-area fraction and mean loaded stress were then examined. Table 2 shows that loaded-area coverage changes only modestly with pressure drop compared with the increase in mean loaded stress. For the normal component on the whole screen, f_L increases from 0.0306 at Δp_1 to 0.0381 at Δp_2 and 0.0385 at Δp_3, whereas μ_{active} increases from 6,674 to 11,378 and 21,256 Pa. For the shear component, f_L increases from 0.0272 to 0.0351 and 0.0372, whereas μ_{active} increases from 1,541 to 3,284 and 4,881 Pa. Pressure drop therefore amplifies stress intensity within already engaged regions more strongly than it expands the loaded-area coverage.

In addition, μ_{active} remains well above P75 in all cases, which indicates right-skewed stress distributions even within the stabilised regime. Central statistics therefore characterise the typical loading state but do not resolve how the most severe stresses evolve with pressure drop. Upper-percentile and exceedance metrics are examined next to determine whether increasing pressure drop produces near-uniform amplification or preferential growth of extreme stresses.

3.3 Upper-tail and exceedance behaviour

Upper-tail behaviour is now examined using conditional loaded-area exceedance and very-high-tail percentiles, which complement the bulk percentile shifts in Fig. 3. Fig. 4 presents the conditional loaded-area exceedance, $E_{\text{loaded}}(\sigma \geq T)$, for each reporting zone and stress component.

For all zones and both stress components, $E_{\text{loaded}}(\sigma \geq T)$ decreases monotonically with increasing threshold T. As pressure drop increases, however, this decay becomes less steep. At any fixed threshold, a larger pressure drop therefore yields a larger fraction of high-stress samples within the loaded area. Pressure drop thus acts not only on the typical loading level but also on the fraction of probability mass that occupies the upper tail.

For the normal component at $T = 2{,}000$ Pa, whole-screen exceedance increases from 0.1587 at Δp_1 to 0.2181 at Δp_2 and 0.4136 at Δp_3. The increment from Δp_2 to Δp_3 exceeds that from Δp_1 to Δp_2, which indicates a nonlinear increase in the fraction of loaded area that occupies the high-stress regime at the largest pressure drop. At this threshold, perimeter exceedance exceeds interior exceedance at Δp_1, the separation narrows at Δp_2, and both zones remain strongly engaged at Δp_3. Fixed-threshold exceedance and very-high-tail percentiles do not, however, convey identical information. The threshold-based metric tracks the fraction of area above a moderate fixed level, whereas P99 and P99.5 isolate the most severe end of the loaded-area distribution.

For the shear component at $T = 500$ Pa, whole-screen exceedance increases from 0.1277 at Δp_1 to 0.1554 at Δp_2 and 0.2623 at Δp_3. At Δp_1 and Δp_3, perimeter exceedance exceeds interior exceedance. At Δp_2, interior exceedance, 0.1611, slightly exceeds the perimeter value, 0.1220, which indicates a pressure-dependent reversal in zone ordering at the intermediate pressure drop. Even under this reversal, shear

Table 3. Loaded-area exceedance at the normal and shear reference thresholds.

Case	Normal component, $E(\sigma_n \geq 2{,}000$ Pa)			Shear component, $E(\sigma_5 \geq 500$ Pa)		
	Whole screen	Perimeter zone	Interior zone	Whole screen	Perimeter zone	Interior zone
Δp_1	0.1587	0.4714	0.1442	0.1277	0.3267	0.1184
Δp_2	0.2181	0.2579	0.2113	0.1554	0.122	0.1611
Δp_3	0.4136	0.6146	0.4006	0.2623	0.5214	0.2455

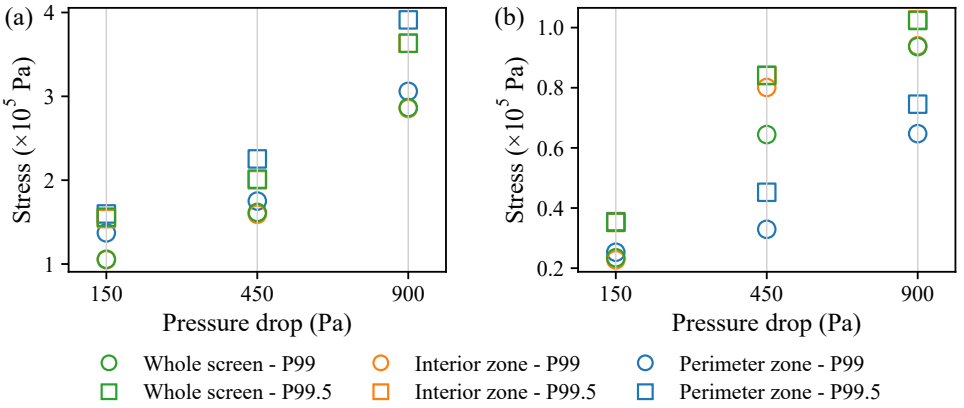

Fig. 5. Upper-tail percentiles versus pressure drop for stabilised (a) normal and (b) shear stresses.

tails remain thinner than the corresponding normal tails at their respective anchor thresholds, which is consistent with the normal-dominated hierarchy identified earlier through P50 and P75.

To examine whether pressure-drop amplification extends into the most severe part of the loaded-area distribution, upper-tail behaviour was assessed using extreme percentiles. Fig. 5 summarises tail severity through P99 and P99.5 across zones and pressure drops. For both stress components and all zones, P99 and P99.5 increase with pressure drop. The separation between P99 and P99.5 also widens at higher pressure drop, which indicates increased dispersion within the extreme tail rather than rigid translation of the entire distribution. This behaviour matches the reduced steepness observed in Fig. 4 and confirms that pressure-drop amplification is strongest in the most severe part of the loaded-area distribution.

For the normal component, the added corner split of the 10% perimeter band shows that the elevated upper tail is not confined to corner facets. The non-corner perimeter region exceeds the interior in both P99 and P99.5 across all three pressure-drop cases, whereas the corner subset carries the strongest extremes, as shown in Figs. S4(a) and S4(b). The normal upper tail is therefore interpreted as a perimeter-associated feature under the present configuration rather than as a corner-only effect. Table 3 lists the loaded-area exceedance values at the reference thresholds used in Fig. 4, namely 2,000 Pa for the normal component and 500 Pa for the shear component.

Taken together, the results show that pressure drop intensifies stabilised loading through two coupled responses. Typical loading increases primarily through amplification of stress intensity within the loaded area, whereas the upper tail also strengthens. Very-high-tail percentiles show perimeter-associated amplification in the normal component, whereas fixed-threshold exceedance does not indicate perimeter dominance in every case because the interior can occupy a larger fraction of moderately high-stress area once the overall loading level rises. A supporting sensitivity check further shows that this perimeter-associated normal upper-tail effect remains qualitatively consistent for the 10% and 15% perimeter-band definitions, whereas a 5% band is too narrow to capture the full engaged perimeter zone, as shown in Figs. S4(d) to S4(f).

3.4 Zone contrast explained by loaded area and mean loaded stress

Perimeter-interior contrasts in the upper tail may be interpreted through the same decomposition used for the bulk loading state, namely the loaded-area fraction f_L and the mean loaded stress μ_{active}. Table 2 provides this decomposition for the normal and shear components across the three pressure-drop cases.

For the normal component at Δp_1, the perimeter exhibits a smaller loaded-area fraction than the interior, 0.0094 versus 0.0343, but a substantially larger mean loaded stress, 14,418 versus 6,298 Pa. The perimeter therefore carries higher stress intensity over a smaller engaged area. This is consistent with the stronger perimeter-associated high-tail statistics reported in Section 3.3. At Δp_2, the loaded-area fractions become similar, 0.0355 versus 0.0386, whereas the interior exhibits the larger

mean loaded stress, 12,304 versus 5,936 Pa. This reversal in μ_{active} coincides with the reduced separation in the normal upper-tail metrics at the intermediate pressure drop. At Δp_3, the perimeter loaded-area fraction decreases to 0.0156 while the interior increases to 0.0425. However, perimeter μ_{active} rises 29,868 Pa, which exceeds the interior value of 20,696 Pa. The perimeter therefore again carries higher stress intensity over a relatively small engaged area, which aligns with the stronger perimeter-associated normal P99 and P99.5 values even though fixed-threshold exceedance remains substantial in both zones.

Across pressure drops, the perimeter does not consistently exhibit larger loaded-area fraction. The decisive variable is the relative magnitude of μ_{active}. When perimeter μ_{active} exceeds interior μ_{active}, the most severe normal tail strengthens in the perimeter-associated regions. When it is lower, the separation narrows or reverses.

The same decomposition clarifies the shear-component ordering. At Δp_1, the perimeter has a smaller loaded-area fraction than the interior, 0.0076 versus 0.0306, but a higher mean loaded stress, 2,692 versus 1,491 Pa, which is consistent with higher perimeter exceedance at 500 Pa. At Δp_2, the loaded-area fractions are similar, 0.0334 versus 0.0354, whereas the interior mean loaded stress exceeds that of the perimeter, 3,630 versus 1,304 Pa. This reversal is confined to the fixed-threshold shear exceedance metric and should not be interpreted as a wholesale inversion of the shear loading hierarchy. It instead indicates that, at the intermediate pressure drop, a somewhat larger interior area lies above the moderate 500 Pa threshold. Threshold-based area coverage and upper-tail intensity are different descriptors, so this result is more consistent with broader interior recruitment into the moderate shear-loading regime than with clear interior dominance of the severe shear tail. At Δp_3, the perimeter loaded-area fraction decreases to 0.0154 while the interior increases to 0.0410, but the perimeter mean loaded stress rises to 6745 Pa compared with 4757 Pa in the interior. This intensity contrast aligns with renewed perimeter strengthening in the shear exceedance metrics, although the shear response remains less systematic than the normal response.

Zone contrasts in the upper tail therefore do not follow loaded-area fraction alone. Loaded-area fractions vary modestly and do not show persistent perimeter dominance. Instead, the strongest normal tail follows where μ_{active} is largest. At the same time, fixed-threshold exceedance and very-high-tail percentiles should not be conflated. The perimeter-associated regions carry the most severe normal tail, whereas the interior can still occupy a larger fraction of moderately high-stress area at some pressure drops. A supporting loaded-threshold sensitivity check further showed that increasing $\sigma_{\min}$ from 0 to 1 Pa produced only negligible changes in f_L and μ_{active} and did not alter the weighted quantiles or exceedance-based ordering, as reported in Table S3. The decomposition is therefore not sensitive to the zero-threshold choice. The next subsection examines hotspot maps to show how these intensity-driven contrasts manifest spatially across the screen surface and how high-stress coverage evolves with pressure drop.

3.5 Spatial organisation of hotspot fields in the stable regime

The preceding decomposition showed that perimeter-associated tail strengthening follows differences in stress intensity when perimeter μ_{active} exceeds interior μ_{active}, whereas f_L does not exhibit systematic perimeter dominance across pressure drops. Spatial fields are now examined together with within-window summary statistics in order to characterise both temporal variability and hotspot morphology inside the stable window. Fig. 6 summarises the stable-window median and interquartile range of the per-time P99 series, the corresponding whole-screen anchor exceedance E_{zone}, and the dominant-cluster continuity metric C_{dom}. The representative snapshot is the time at which the per-time P99 is closest to the stable-window median, whereas the elevated snapshot is the time at which the per-time P99 is closest to the stable-window 90-th percentile. Figs. 7 and 8 show these statistically anchored representative and elevated hotspot maps for the normal and shear components. The hotspot maps are interpreted as loading-concentration fields on the rigid reference PW geometry, not as direct predictions of local wire deformation or failure.

The within-window summaries support the visual hotspot interpretation. Fig. 6 shows that the stable-window median P99 and whole-screen anchor exceedance both increase monotonically with pressure drop for the normal and shear components, whereas their interquartile spans remain small relative to the cross-case separation. The representative and elevated snapshot markers lie close to the corresponding central and upper-window levels, which confirms that the selected frames were not visually hand-picked.

By contrast, dominant-cluster continuity does not increase monotonically with pressure drop. For the normal component, the median C_{dom} decreases from 0.124 at Δp_1 to 0.063 at Δp_2 and 0.024 at Δp_3. For the shear component, it increases from 0.0059 at Δp_1 to 0.102 at Δp_2 and then decreases to 0.0457 at Δp_3. Higher pressure drop therefore expands the area above the anchor threshold more clearly than it consolidates that area into a single dominant connected hotspot cluster.

For the normal component at Δp_1, high-stress regions are sparse and spatially localised. In the representative snapshot, P99 = 2.06×10^5 Pa and $E(\sigma_n \geq 2{,}000\text{Pa}) = 7.81 \times 10^{-2}$. In the elevated snapshot, P99 remains 2.06×10^5 Pa and the exceedance fraction increases slightly to 8.25×10^{-2}. The spatial pattern is effectively unchanged between the two states, and this visual persistence is consistent with the narrow within-window spreads of P99, E_{zone}, and C_{dom} reported in Fig. 6. Elevated loading at this pressure therefore reflects intensity modulation within an already sparse load-bearing structure, which is also consistent with the modest change in f_L reported in Table 2.

At Δp_2, extreme percentiles and exceedance increase substantially. The representative snapshot gives P99 = 3.55×10^5 Pa and $E = 1.29 \times 10^{-1}$, whereas the elevated snapshot gives P99 = 3.58×10^5 Pa and $E = 1.63 \times 10^{-1}$. Relative to Δp_1, high-stress regions occupy a larger fraction of the surface. Representative and elevated fields at Δp_2 remain geometrically similar, and the main difference between them is quantitative

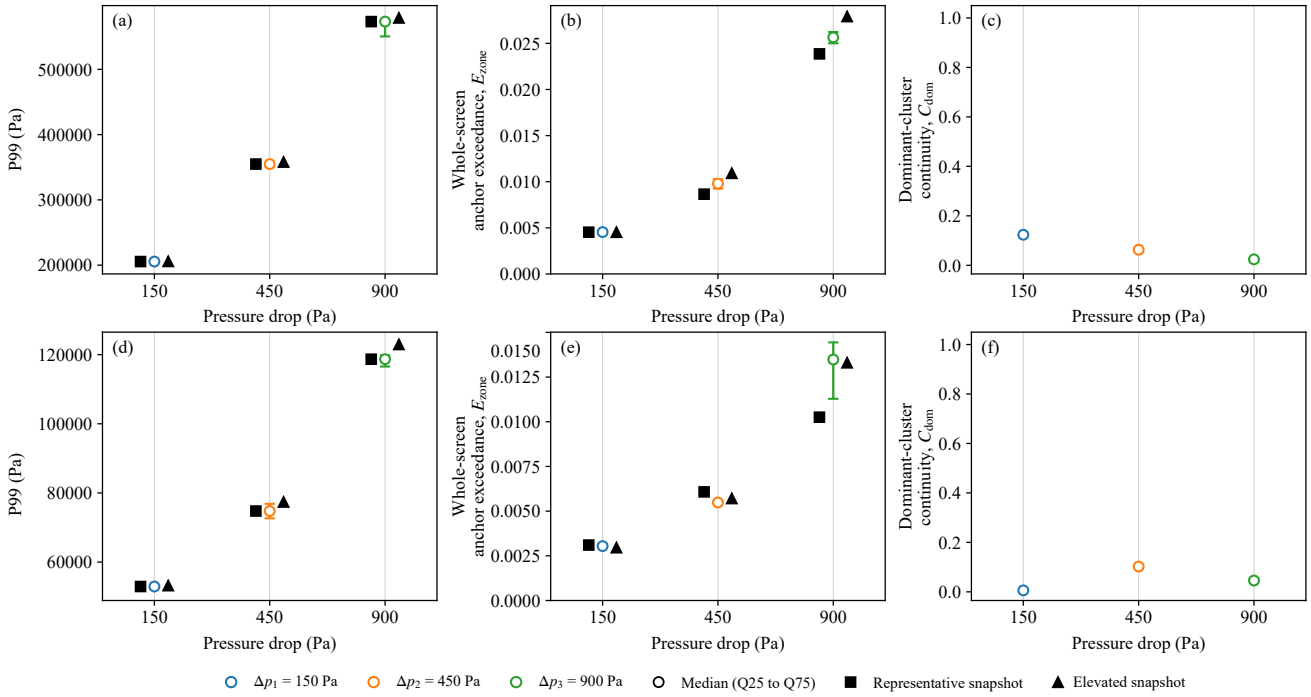

Fig. 6. Within-window summaries across pressure-drop cases for (a) normal-stress P99, (b) anchor exceedance, (c) normal dominant-cluster continuity, and (d)-(f) shear-stress counterparts.

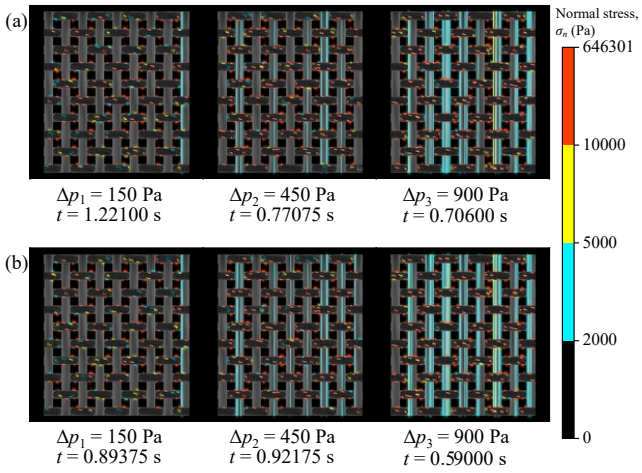

Fig. 7. (a) Representative and (b) elevated stabilised-window hotspot maps for the normal component.

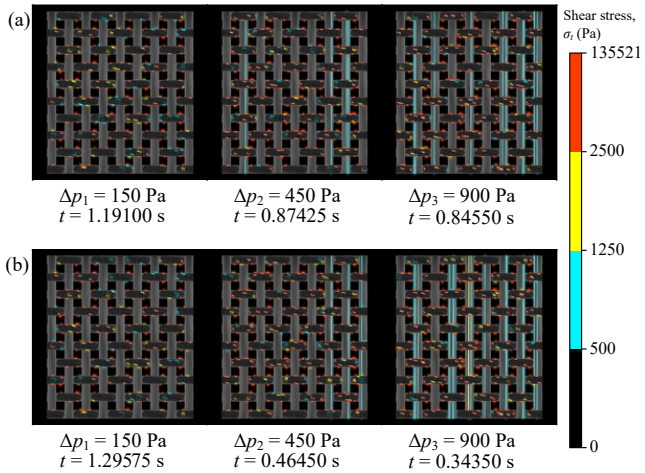

Fig. 8. (a) Representative and (b) elevated stabilised-window hotspot maps for the shear component.

rather than organisational. Fig. 6 further shows that the within-window spread in C_{dom} at Δp_2 is narrow, even though its median level is lower than at Δp_1. Such a behaviour matches the upper-tail thickening identified earlier in Figs. 4 and 5.

At Δp_3, hotspot extent increases further. In the representative snapshot, P99 = 5.73×10^5 Pa and $E = 3.21 \times 10^{-1}$. In the elevated snapshot, P99 = 5.79×10^5 Pa and $E = 3.76 \times 10^{-1}$. Compared with Δp_2, the increase in exceedance indicates that extreme normal stresses occupy a substantially larger fraction of the surface. The hotspot alignment with weave features in Figs. 7 and 8 is consistent with geometric amplification near structural discontinuities and intersections (Inglis, 1913; Medina et al., 2015; Patel and Desai, 2020). This provides the spatial counterpart of the nonlinear increase in upper-tail mass identified earlier from the exceedance increments between Δp_2 and Δp_3.

The shear component follows the same pressure ordering but with lower absolute magnitudes and smaller exceedance at the reference threshold. At Δp_1, the representative snapshot gives P99 = 5.29×10^4 Pa and $E(\sigma_t \geq 500\ \text{Pa}) = 5.40 \times 10^{-2}$, whereas the elevated snapshot gives P99 = 5.32×10^4 Pa and $E = 5.16 \times 10^{-2}$. Hotspots are fragmented and confined to small regions, and the spatial pattern remains stable between representative and elevated states. At Δp_2, P99 increases to 7.48×10^4 Pa in the representative state and 7.74×10^4 Pa in the elevated state. The exceedance fraction remains close to 9×10^{-2}, with $E = 9.07 \times 10^{-2}$ in the representative snapshot and $E = 8.72 \times 10^{-2}$ in the elevated snapshot. Shear

hotspots become more extensive than at Δp_1 but remain less extensive than the corresponding normal-stress regions. At Δp_3, the representative snapshot yields P99 = 1.19×10^5 Pa and $E = 1.39 \times 10^{-1}$, whereas the elevated snapshot yields P99 = 1.23×10^5 Pa and $E = 1.80 \times 10^{-1}$. Shear hotspots therefore expand markedly relative to the lower pressure-drop cases, although the median shear C_{dom} at Δp_3 remains below the corresponding value at Δp_2. Higher shear exceedance at Δp_3 therefore reflects broader hotspot coverage rather than stronger dominance of a single connected cluster.

Taken together, the hotspot fields provide the spatial manifestation of the statistical trends established earlier. Pressure drop increases typical loading primarily through stress-intensity amplification within the loaded area, and it also strengthens the upper tail. The strongest normal extremes remain associated with the perimeter band, whereas the interior can still occupy a larger fraction of area above a moderate fixed threshold in some cases. The added corner split shows that the elevated normal upper tail is not confined to corners under the baseline 10% band definition, although corners do concentrate the largest exceedance fractions, as shown in Figs. S4(a) to S4(c). The hotspot fields are therefore interpreted as consistent with a perimeter-associated high-tail response under the present configuration, and not as proof that boundary effects are fully excluded.

3.6 Implications for sustained loading and failure relevance

Overall, Sections 3.2-3.5 establish a consistent stabilised response to pressure drop. Bulk statistics show that typical loading rises monotonically with Δp, and the dominant contribution comes from growth of stress intensity within the loaded area, whereas systematic expansion of the loaded fraction plays a secondary role. Tail statistics show that the upper distribution also strengthens as Δp increases, and zone-level contrasts arise primarily from differences in μ_{active} rather than persistent perimeter dominance in f_L. The strongest normal tail is associated with the perimeter band under the present configuration, although fixed-threshold exceedance shows that the interior can still occupy a substantial fraction of moderately high-stress area at higher pressure drop. The within-window summary further shows that cross-case strengthening in P99 and whole-screen anchor exceedance exceeds the corresponding within-window spread, whereas dominant-cluster continuity remains case-stable but non-monotonic across pressure drop. Sensitivity checks showed that the main conclusions were insensitive to the loaded-facet threshold, as reported in Table S3, and were qualitatively consistent for the 10% and 15% perimeter-band definitions, whereas a 5% band underresolved the engaged perimeter loading zone, as shown in Fig. S4.

The present analysis therefore contributes a loading-side framework that separates typical loading, extreme loading, and spatial organisation under mechanically comparable stabilised states. Loaded-area conditioning avoids conflating unloaded facets with low-stress facets, the $f_L - \mu_{\text{active}}$ decomposition separates area recruitment from stress-intensity amplification, and tail percentiles and exceedance curves quantify severe loading without reliance on isolated maxima. The hotspot summaries add a spatial counterpart to these distribution-level metrics by distinguishing broader hotspot coverage from consolidation into a single dominant connected cluster.

From a screen-survivability perspective, the present metrics should be interpreted as loading descriptors rather than direct failure criteria. Elevated normal tails and large normal exceedance indicate stronger local compressive and bearing-type demand on wires and intersections, whereas elevated shear tails and broader shear hotspot coverage indicate stronger tangential demand that may be relevant to sliding, fretting, or wear-prone response. However, yielding, fatigue, collapse, and erosion failure also depend on material properties, wire support conditions, structural compliance, cyclic load history, and environment. Direct failure assessment therefore requires explicit coupling of the present loading descriptors to a structural-response model and material-specific limits.

4. Conclusions

This study quantified loading-induced normal and shear stresses on a PW standalone screen beneath stabilised sand filter-beds for three imposed pressure drops, namely $\Delta p_1 = 150$ Pa, $\Delta p_2 = 450$ Pa, and $\Delta p_3 = 900$ Pa. A resolved immersed-boundary CFD-DEM framework was used to map fluid traction and particle-contact loading onto screen-surface facets. Stress statistics were pooled over deterministically identified stabilised windows so that cross-case comparisons represented mechanically comparable filter-bed states.

Pressure drop produced a clear monotonic strengthening of the stabilised loading state. For the whole screen, the normal-component median increased from 413 Pa at Δp_1 to 824 Pa at Δp_2 and 1,631 Pa at Δp_3, whereas the shear-component median increased from 70 to 123 and 272 Pa. Normal stresses therefore dominated throughout. The loaded-area fraction increased only modestly, with f_L rising from 0.0306 to 0.0385, whereas the mean stress over the loaded area increased strongly, with μ_{active} rising from 6,674 to 21,256 Pa. Pressure drop therefore amplified stress intensity within already engaged regions more strongly than it expanded engaged area.

Extreme loading also strengthened with pressure drop, although the zone-level interpretation depended on the metric used. Loaded-area exceedance increased from 0.1587 to 0.4136 at 2,000 Pa for the normal component and from 0.1277 to 0.2623 at 500 Pa for the shear component. Very-high-tail percentiles and fixed-threshold exceedance did not show identical zone ordering. The most severe normal tail was associated with the perimeter band under the present configuration, whereas the interior could still occupy a larger fraction of moderately high-stress area at some pressure drops. A corner split of the baseline 10% perimeter band showed that the elevated normal upper tail was not confined to corners, because the non-corner perimeter region exceeded the interior in P99 and P99.5 across all three pressure-drop cases, whereas corners concentrated the strongest exceedance fractions.

Sensitivity checks supported the robustness of the loading

descriptors. Increasing the loaded-facet threshold from 0 to 1 Pa produced only negligible changes in f_L and μ_{active} and did not alter weighted quantiles or exceedance-based ordering. Varying the perimeter-band width showed that the normal upper-tail interpretation was qualitatively consistent for the 10% and 15% definitions, whereas a 5% band under-resolved the engaged perimeter loading zone. The results therefore support a perimeter-associated normal upper-tail response under the present configuration, while not claiming that boundary effects are fully excluded.

Within-window summary metrics further showed that the stable-window spread of P99 and whole-screen anchor exceedance was smaller than the cross-case strengthening induced by increasing pressure drop. Dominant-cluster continuity, however, did not increase monotonically with pressure drop. Higher forcing enlarged hotspot area above the anchor thresholds more clearly than it consolidated that area into a single dominant connected cluster.

Taken together, these results establish a mechanics-based framework for sustained screen loading under stabilised filter-bed conditions that separates typical loading, extreme loading, and spatial organisation. Percentile and exceedance measures quantify severe loading without reliance on isolated maxima, the $f_L - \mu_{\text{active}}$ decomposition separates area recruitment from stress-intensity amplification, and the within-window hotspot summaries distinguish broader hotspot coverage from consolidation into a single connected cluster. These outcomes therefore provide loading-side inputs that can support comparative screen qualification and conservative operating-envelope assessment for premium standalone screens under stabilised filter-bed loading. They are not direct failure criteria, because yielding, fatigue, fretting, collapse, and erosion also depend on material properties, wire support conditions, structural compliance, cyclic load history, and environment. Future work should therefore couple the present loading descriptors to deformable wire-network or structural-response models with material-specific limits, test sensitivity to alternative stochastic initialisations, extend the framework to other screen architectures, and examine broader particle-size distributions with non-spherical grains and richer fines content so that stabilised loading descriptors can be linked more directly to integrity-relevant failure modes.

Acknowledgements

Financial support for this work was provided by Universiti Teknologi Brunei through funding for sand retention mitigation research. UNSW Sydney provided financial assistance towards R. R.'s tuition fees. The authors also acknowledge technical input from Imperial College London, which contributed to improving the quality of the study. Computational resources were provided by the Katana high-performance computing cluster, supported by Research Technology Services at UNSW Sydney (DOI: 10.26190/669X-A286).

Supplementary file

https://doi.org/10.46690/ager.2026.05.02

Conflicts of interest

The authors declare no competing interest.

References

Abduljabbar, A., Amadi, A., Mohyaldinn, M. E., et al. Sand screens application and performance for sand control: A review of selection criteria, screen materials, and causes of failure. Heliyon, 2024, 10: e30731.

Adams, P. R., Davis, E. R., Hodge, R. M., et al. Current state of the premium screen industry: Buyer beware - methodical testing and qualification shows you do not always get what you paid for. Paper SPE 110082 Presented at SPE Annual Technical Conference and Exhibition, Anaheim, California, USA, 11-14 November, 2007.

Ahad, N. A., Jami, M., Tyson, S. A review of experimental studies on sand screen selection for unconsolidated sandstone reservoirs. Journal of Petroleum Exploration and Production Technology, 2020, 10: 1675-1688.

Arukhe, J., Uchendu, C., Nwoke, L. Horizontal screen failures in unconsolidated, high-permeability sandstone reservoirs: Reversing the trend. Paper SPE-97299-MS Presented at SPE Annual Technical Conference and Exhibition, Dallas, Texas, USA, 9-12 October, 2005.

Brilliantov, N. V., Spahn, F., Hertzsch, J. M., et al. Model for collisions in granular gases. Physical Review E, 1996, 53: 5382-5392.

Cundall, P. A., Strack, O. D. L. A discrete numerical model for granular assemblies. Geotechnique, 1979, 29: 47-65.

DCS Computing GmbH. LIGGGHTS-PUBLIC user's manual (version 3.X), 2013.

Goniva, C., Kloss, C., Hager, A., et al. An open-source CFD-DEM perspective. Paper Presented at 5th OpenFOAM Workshop, Gothenburg, Sweden, 21-24 June, 2010.

Goniva, C., Kloss, C., Pirker, S. Towards fast parallel CFD-DEM: An open-source perspective. Paper Presented at Open Source CFD International Conference, Barcelona, Spain, 12-13 November, 2009.

Greenwood, J. A., Williamson, J. B. P. Contact of nominally flat surfaces. Proceedings of the Royal Society of London Series A, 1966, 295: 300-319.

Hager, A., Kloss, C., Goniva, C. Towards an efficient immersed boundary method within an open source framework. Presented at 12th International Conference on Multiphase Flow in Industrial Plants, Ischia (Napoli), Italy, 21-23 September, 2011.

Hager, A., Kloss, C., Goniva, C. Parallel open source CFD-DEM for resolved particle-fluid interaction. Paper Presented at Ninth International Conference on Computational Fluid Dynamics in Minerals and Process Industries, Melbourne, Australia, 10-12 December, 2012.

Hager, A., Kloss, C., Pirker, S., et al. Parallel resolved open source CFD-DEM: Method, validation and application. Journal of Computational Multiphase Flows, 2014, 6: 13-

27.

Hamid, S., Ali, S. A. Causes of sand control screen failures and their remedies. Paper SPE 38190 Presented at SPE European Formation Damage Conference and Exhibition, The Hague, The Netherlands, 2-3 June, 1997.

Inglis, C. E. Stresses in plates due to the presence of cracks and sharp corners. Transactions of the Institute of Naval Architects, 1913, 55: 219-241.

Joe, J., Wang, A., Barber, J. R. Load-displacement relation and gap distribution between rough surfaces: Partial differential equations approach. Journal of the Mechanics and Physics of Solids, 2023, 180: 105397.

Kloss, C., Goniva, C., Hager, A., et al. Models, algorithms and validation for open-source DEM and CFD-DEM. Progress in Computational Fluid Dynamics, 2012, 12: 140-152.

Majmudar, T. S., Behringer, R. P. Contact force measurements and stress-induced anisotropy in granular materials. Nature, 2005, 435: 1079-1082.

Medina, H. E., Pidaparti, R., Hinderliter, B. Celebrating the 100th anniversary of Inglis result: From a single notch to random surface stress concentration solutions. Applied Mechanics Reviews, 2015, 67: 010802.

Meng, Q., Song, H., Zhou, Y., et al. Unifying linear proportionality between real contact area and load in rough surface contact. Journal of the Mechanics and Physics of Solids, 2025, 196: 105975.

Patel, A., Desai, C. K. Stress concentration around an elliptical hole in a large rectangular plate subjected to linearly varying in-plane loading on two opposite edges. Theoretical and Applied Fracture Mechanics, 2020, 106: 102432.

Persson, B. N. J. Elastoplastic contact between randomly rough surfaces. Physical Review Letters, 2001, 87: 116101.

Peskin, C. S. The immersed boundary method. Acta Numerica, 2002, 11: 479-517.

Peters, J. F., Muthuswamy, M., Wibowo, J., et al. Characterization of force chains in granular material. Physical Review E, 2005, 72: 041307.

Procyk, A., Gou, X., Marti, S. K., et al. Sand control screen erosion: Prediction and avoidance. Paper SPE 174837 Presented at SPE Annual Technical Conference and Exhibition, Houston, Texas, USA, 28-30 September, 2015.

Razak, R., Alosail, M. S., Musa, K. I., et al. Spatially resolved CFD-DEM model with innovative experimental validation methods to improve understanding of sand retention in oil and gas wells with the consideration of filter-beds on standalone screens. Powder Technology, 2024, 449: 120406.

Razak, R., Gago, P. A., Chen, Z., et al. Influence of weave geometry and layering on the progression of sand retention and permeability in standalone screens using resolved CFD-DEM. International Journal of Multiphase Flow, 2025, 194: 105481.

Shirgaonkar, A. A., MacIver, M. A., Patankar, N. A. A new mathematical formulation and fast algorithm for fully resolved simulation of self-propulsion. Journal of Computational Physics, 2009, 228: 2366-2390.

Taira, K., Colonius, T. The immersed boundary method: A projection approach. Journal of Computational Physics, 2007, 225: 2118-2137.

van Eerd, A. R. T., Ellenbroek, W. G., van Hecke, M., et al. Tail of the contact force distribution in static granular materials. Physical Review E, 2007, 75: 060302.

Weller, H. G., Tabor, G., Jasak, H., et al. A tensorial approach to computational continuum mechanics using object-oriented techniques. Computers in Physics, 1998, 12: 620-631.

Wong, G. K., Fair, P. S., Bland, K. F., et al. Balancing act: Gulf of Mexico sand control completions, peak rate versus risk of sand control failure. Paper SPE 84497 Presented at SPE Annual Technical Conference and Exhibition, Denver, Colorado, USA, 5-8 October, 2003.

Ying, R., Zhao, X., Shi, B., et al. Experimental study on erosion and wear law of metal screen under spraying condition. Journal of Mechanics, 2022, 38: 117-127.

Zhang, L., Wang, Y., Zhang, J. Force-chain distributions in granular systems. Physical Review E, 2014, 89: 012203.

Zhang, R., Hao, S., Zhang, C., et al. Analysis and simulation of erosion of sand control screens in deep water gas well and its practical application. Journal of Petroleum Science and Engineering, 2020, 189: 106997.

Zhou, B., Dong, C., Gan, L., et al. Experimental simulation and new prediction model of sand control screen erosion performance in weakly consolidated heterogeneous reservoirs. Journal of Petroleum Science and Engineering, 2022, 215: 110587.